ACCSCIENCE PUBLISHING

Materials Science in Additive Manufacturing

ORIGINAL RESEARCH ARTICLE

Blast resistance of polyurethane-filled 316L stainless steel honeycomb sandwich structures fabricated by selective laser melting

Xingran Zheng[1,2], Jingbo Huang[1,2], Xiaoshuai Li[1], Liangjun Ma[1,2], Chao Zhang[3], Yangwei Wang[4], Pengwan Chen[1,2], and Jing Xie[1,2]*

[1]State Key Laboratory of Explosion Science and Safety Protection, Beijing Institute of Technology, Beijing, China

[2]Yangtze Delta Region Academy of Beijing Institute of Technology, Jiaxing, Zhejiang, China

[3]School of Water Conservancy and Transportation, Yellow River Laboratory, Underground Engineering Research Institute, Zhengzhou University, Zhengzhou, Henan, China

[4]National Key Laboratory of Science and Technology on Materials Under Shock and Impact, Beijing, China

***Corresponding author:**
Jing Xie
(jxie@bit.edu.cn)

Citation: Zheng X, Huang J, Li X, *et al*. Blast resistance of polyurethane-filled 316L stainless steel honeycomb sandwich structures fabricated by selective laser melting. *Mater Sci Add Manuf.* 2026;5(3):025480112. doi: 10.36922/MSAM025480112

Received: November 25, 2025

1st revised: January 22, 2026

2nd revised: June 15, 2026

Accepted: June 23, 2026

Published online: July 21, 2026

Copyright: © 2026 Author(s). This is an Open-Access article distributed under the terms of the Creative Commons Attribution License, permitting distribution, and reproduction in any medium, provided the original work is properly cited.

Publisher's Note: AccScience Publishing remains neutral with regard to jurisdictional claims in published maps and institutional affiliations.

Abstract

Honeycomb sandwich structures (HSS) have attracted increasing attention for blast protection because of their lightweight characteristics, high specific strength, and excellent energy absorption capacity; however, the near-field blast response and component-level energy absorption mechanisms of integrated metal–polymer honeycomb structures remain insufficiently understood. In this study, a blast-resistant HSS fabricated by selective laser melting (SLM) using 316L stainless steel and filled with polyurethane (PU) was designed and experimentally investigated under near-field explosion loading. Three scaled distances of Z = 0.1315, 0.1972, and 0.2630 m•kg$^{-1/3}$ were tested to evaluate the blast resistance and energy absorption characteristics of the PU-filled SLM HSS compared with an equivalent areal-density solid plate. The mechanical tests were conducted on SLM-fabricated 316L stainless steel, and the Johnson–Cook constitutive parameters were calibrated from the measured stress–strain responses. A coupled fluid–structure interaction numerical model based on the S-ALE algorithm in LS-DYNA was established and validated against experiments. Results show that the PU-filled HSS exhibits markedly smaller back-face deflection and improved blast resistance compared to the solid plate. At the closest stand-off distance, the back-face residual deflection of the HSS decreased by 20.4%, indicating that the honeycomb core and PU filling effectively attenuate transmitted impact energy. Across the tested stand-off distances, the honeycomb core and PU filling contributed 44.6–46.3% and 22.7–25.5% of the total absorbed energy, respectively. The combined mechanisms of plastic buckling, viscoelastic dissipation, and micropore compression endow the composite core with superior energy absorption efficiency and structural integrity under extreme loading. This study provides an effective design strategy for lightweight, high-performance blast-resistant sandwich structures.

Keywords: Honeycomb sandwich structure; Selective laser melting; Polyurethane; Wave propagation; Mechanical response

1. Introduction

Honeycomb sandwich structures (HSS) are widely applied in aerospace, aviation, marine, and automotive industries due to their high specific strength, excellent sound and vibration insulation, superior impact resistance, and remarkable energy absorption capability.[1] A typical HSS configuration consists of two face sheets and a central honeycomb core, where both the face sheets and core can be fabricated from various materials such as metals, ceramics, or composites.[2-4] The core layer can be designed in lattice, grid, or even auxetic configurations.[5-7] The high customizability of both materials and architectures enables HSS to demonstrate great potential in explosion protection and energy absorption applications.

In recent years, extensive research has been conducted on the dynamic response of metallic sandwich structures under explosive loading. Dharmasena *et al.*[8] carried out air-blast experiments on stainless steel honeycomb sandwich plates and found that the back-face deflection decreased to 40% of that of a solid plate at low impulse levels, indicating that the honeycomb core can effectively mitigate shock transmission. Yungwirth *et al.*[9] reported that the transmitted shock intensity of a pyramidal lattice-core sandwich panel was reduced by approximately 28% compared to an equal-areal-density solid plate, further verifying the advantage of honeycomb structures in attenuating impact loads. Bohara *et al.*[10] designed a dual-mechanism auxetic sandwich structure that absorbed 2.69 times more energy and produced nearly 50% less residual back-face deflection under blast loading, demonstrating the superior protective performance of novel porous cores. Yazici *et al.*[11] and Alavi and Sadeghi[12] further confirmed the stable energy absorption performance of polyurethane (PU)-filled metallic sandwich structures under moderate to high strain-rate compression, showing significant reductions in front- and back-face deflection with only minor increases in overall mass. By combining experimental tests and numerical simulations, Li *et al.*[13] investigated the performance of graded foam sandwich panels under combined loading conditions. They found that the front face sheet is the key component for dissipating kinetic energy, and that a low–high–medium core gradient configuration most effectively enhances the blast resistance of the structure. More recently, Pan *et al.*[14] found that the energy absorption capacity of PU-filled aluminum hemispherical sandwich panels increased by about 22% compared to that of an equal areal density solid plate, while stress concentration was alleviated.

Overall, metallic HSS can significantly enhance blast resistance while maintaining lightweight characteristics. These advantages mainly arise from three aspects: (i) the fluid–structure interaction effect, which reduces the momentum impulse transmitted to the structure; (ii) the plastic energy absorbed during the crushing deformation of the honeycomb core; and (iii) the increased bending resistance provided by the sandwich configuration.[15] However, conventional honeycomb structures may still suffer from local buckling, core–face debonding, and other failure modes under severe blast loading. Traditional foam fillings generally provide weak lateral support to metallic core webs, which leads to insufficient stabilization during buckling and limits the overall integrity of the structure.[16,17] Therefore, it is necessary to explore advanced honeycomb designs and material selections to further improve blast resistance.

Selective laser melting (SLM) technology, with its high material utilization and excellent forming precision, enables the integrated manufacturing of HSS, effectively improving the insufficient face–core bonding strength.[18] The mechanical properties of SLM-fabricated 316L stainless steel exhibit directionality.[19] This direction-dependent behavior is often approximated as transverse isotropy[20] because thermal gradients align with the build direction, promoting epitaxial grain growth that preferentially orients microstructural features.[21-23] Compared with conventional 316L alloys, SLM-fabricated 316L demonstrates relatively higher yield strength, mainly due to the increased dislocation density[24] and the presence of fine silicon particles throughout the microstructure.[25] By adjusting printing parameters and scanning strategies, the microstructure of the printed product can be intentionally tailored, thereby modifying its final mechanical response and failure behavior.[26]

Polyurethane possesses a highly tunable chemical structure, and its supramolecular architecture formed through hydrogen bonding and microphase separation gives it a favorable combination of mechanical and energy-dissipation properties. PU exhibits efficient energy absorption, pronounced strain-rate sensitivity, and strong compressibility under high strain rates, along with partial reusability and structural integrity retention. These characteristics make PU particularly suitable for combination with metallic honeycomb frameworks to significantly enhance the overall blast resistance.[27-29] PU elastomers, with their superior and adjustable elastic–mechanical properties and fatigue resistance, are widely used in protection and energy absorption applications. Their energy absorption mechanisms mainly include two aspects: on one hand, the polymer matrix dissipates energy through chain disentanglement, breakage, and crack propagation; on the other hand, closed-cell micropores in the structure absorb energy via wall bending, buckling, collapse, and gas compression processes.[30,31]

To study the blast-resistance mechanisms of protective structures, accurate characterization of explosive loads is essential. However, near-field blast-load measurements are extremely challenging because detonations generate high temperatures and pressures, high-velocity particle flow, and electromagnetic interference within the fireball. These factors can produce pronounced spatial nonuniformity and stochastic fluctuations in the measured blast loads, resulting in considerable data scatter. Consequently, predictive models also show considerable uncertainty within this range.[32] At present, various empirical formulas for air shock waves have been proposed by researchers such as Henrych[33] and Brode,[34] though each has its own applicable range, and substantial discrepancies remain, especially under near-field explosion conditions.[35,36] For scaled distances $Z \leq 0.4$ m·kg$^{-1/3}$, Shin *et al.*[37] and Karlos *et al.*[38] combined numerical simulations to modify the K–B model within $0.053 \leq Z \leq 0.40$ m·kg$^{-1/3}$, allowing better characterization of near-field blast loads from spherical charges. Xiao *et al.*[39] investigated the effects of cylindrical charge properties—aspect ratio, orientation, and initiation configuration—on blast load parameters (peak overpressure and maximum impulse). The results showed that for scaled distances less than 3.9 m·kg$^{-1/3}$, the influence of charge geometry and initiation configuration must be considered.

Despite the growing body of research on metallic HSS and polymer-filled sandwich systems under blast loading, important gaps still exist. Existing studies have mainly focused on conventionally manufactured aluminum or steel sandwich panels subjected to far-field or moderate blast conditions, while the near-field blast resistance of PU-filled 316L stainless steel honeycomb structures fabricated by SLM has received extremely limited attention. Moreover, although SLM enables the fabrication of integrated face–core honeycomb structures with improved interfacial integrity, the combined effects of SLM-fabricated 316L honeycomb cores and PU filling on blast mitigation mechanisms, especially under close-in detonation, have not been systematically investigated through coupled experimental and numerical approaches. In particular, the quantitative energy absorption contributions of individual components in such integrated composite sandwich structures remain insufficiently understood.

Therefore, in this study, honeycomb sandwich specimens with integrated face–core structures were fabricated by SLM using 316L stainless steel and subsequently filled with PU. Near-field explosion experiments were conducted at scaled distances of $Z = 0.1315$, 0.1972, and 0.2630 m·kg$^{-1/3}$. In addition, the mechanical behavior of SLM-fabricated 316L stainless steel produced with the same processing route as the HSS specimens was experimentally characterized, and the corresponding Johnson–Cook parameters were calibrated to improve the reliability of the numerical material description. Based on the S-ALE algorithm in LS-DYNA, a numerical model describing the "initiation–response–energy absorption" process of the 316L stainless steel HSS under near-field blast loading was established. The dynamic mechanical response, energy absorption, and deformation mechanisms of the HSS were analyzed to provide theoretical support for the blast-resistant design of such structures. The novelty of this work lies not only in the fabrication of an integrated SLM 316L HSS filled with PU, but also in quantitatively revealing the coupled metal–polymer energy absorption mechanism under close-in blast loading, including the respective energy contributions of the metallic honeycomb core and PU filling.

2. Materials and methods

2.1. Honeycomb sandwich structure specimen fabrication

In this study, an integrated honeycomb sandwich specimen was fabricated using SLM. The overall dimensions of the specimen are 286 mm × 286 mm × 13 mm, with a core layer measuring 226 mm × 226 mm × 10 mm. The effective blast-resistant area was designed as the central region of 216.5 mm × 216.5 mm to eliminate boundary effects, as illustrated in Figure 1. Both the front and back face sheets are 1.5 mm thick, while the core consists of regular hexagonal honeycomb cells with a wall thickness of 1 mm and a side length of 5 mm. The schematic of the fabrication procedure is shown in Figure 2A.

Both the raw powder and the specimens were prepared by Tianjin LiM Laser Technology Co., Ltd (China). The specimens were fabricated using a laser power of 325 W, a scanning speed of 1,000 mm/s, a hatch spacing of 0.12 mm, and a layer thickness of 0.06 mm. A bidirectional stripe scanning strategy with a stripe width of 10 mm was employed with a 67° rotation between successive layers. The feedstock powder had a particle size distribution ranging from 15 to 53 μm, and its chemical composition conformed to the Chinese national standard for 316L stainless steel (GB/T 20878–2007). The build orientation was aligned with the axial direction of the honeycomb cells. After fabrication, the specimens were subjected to post-processing heat treatment according to the manufacturer's standard procedure to relieve residual stresses. The density of 316L stainless steel is 7.95 g/cm^3. The fabricated honeycomb panel is shown in Figure 2B.

The PU material was supplied by the School of Water

Conservancy and Transportation, Zhengzhou University (Zhengzhou, China), and consisted of two components, Component A and Component B. Component A mainly contains polymeric polyols and surfactants, whereas Component B primarily consists of isocyanates and plasticizers. At room temperature (24 °C), Components A and B were mixed at a volume ratio of 1:1 and rapidly stirred until a homogeneous mixture was obtained. The mixture was then poured into the designated mold and cured for 12 h to obtain a PU material with high molecular weight and a certain degree of crosslinking. The cured PU material was subsequently cut into hexagonal prisms for filling (Figure 2A).[40] The PU filler was inserted into the stainless steel honeycomb cells through an interference-fit assembly, without the use of adhesives or additional interfacial bonding materials. The density of the PU filling is 1.08 g/cm^3. As shown in Figure 2C, the PU filling used in this study was an elastomer containing numerous micropores with diameters ranging from several tens to several hundreds of micrometers. These micropores enabled energy absorption through cell-wall buckling, collapse, and internal gas compression. The average areal density of the HSS was 5.12 g/cm^2, equivalent to that of a 6.44 mm-thick 316L stainless steel solid plate. The front face sheet, honeycomb core, PU filling, and back face sheet accounted for 1.19 g/cm^2 (23.2%), 2.11 g/cm^2 (41.2%), 0.63 g/cm^2 (12.3%), and 1.19 g/cm^2 (23.2%), respectively.

2.2. Near-field explosion experiment

The top and bottom face sheets of the HSS specimens were extended and perforated, and spacers were placed between them. In the case of the solid plate, the extensions were added only along the outer edges, where perforations were introduced for clamping. Each specimen was secured to the test rig using a fixed frame. The explosive assembly consisted of a cylindrical trinitrotoluene (TNT) charge (Beijing Institute of Technology, China) and a No. 8 detonator (Beijing Institute of Technology, China). The experimental setup is shown in Figure 3.

The cylindrical TNT charge had a density of approximately 1.63 g/cm^3, a mass of 55 g, and a length-to-diameter ratio of 1:1. Three stand-off distances (the distance from the geometric center of the charge to the specimen front surface) were tested: 50 mm, 75 mm, and 100 mm, corresponding to scaled distances of Z = 0.1315, 0.1972, and 0.2630 m·kg$^{-1/3}$, respectively. Test conditions are abbreviated as “H50,” “H75,” “H100” for the HSS specimens. Equivalent areal-density 316L stainless steel solid plate control tests are labeled as “S50,” “S75,” “S100.” Six effective tests were performed in total.

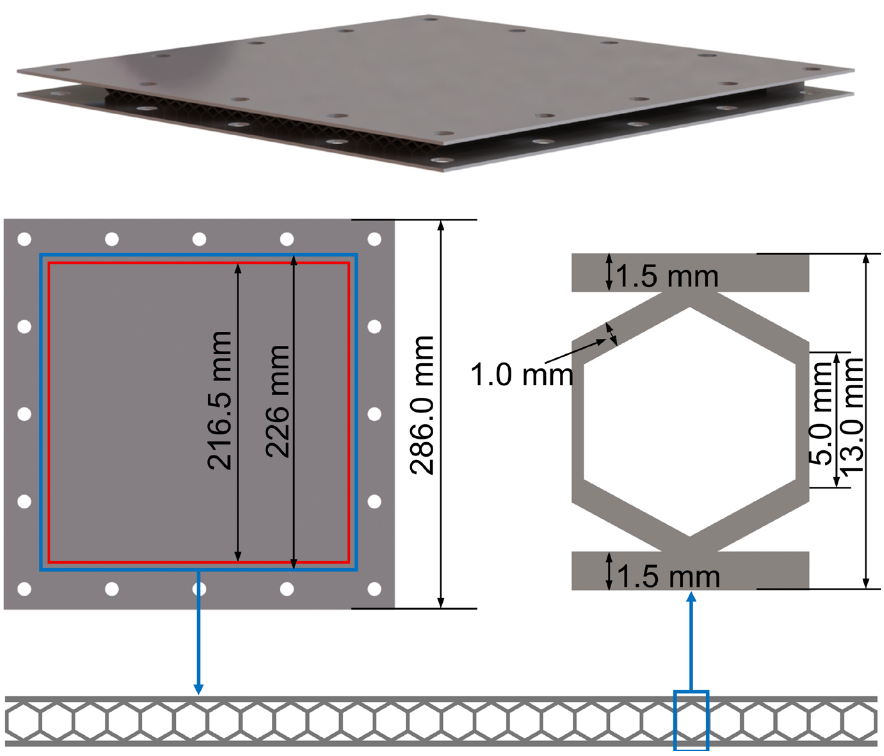

Figure 1. Geometric configuration and dimensions of the honeycomb sandwich structure

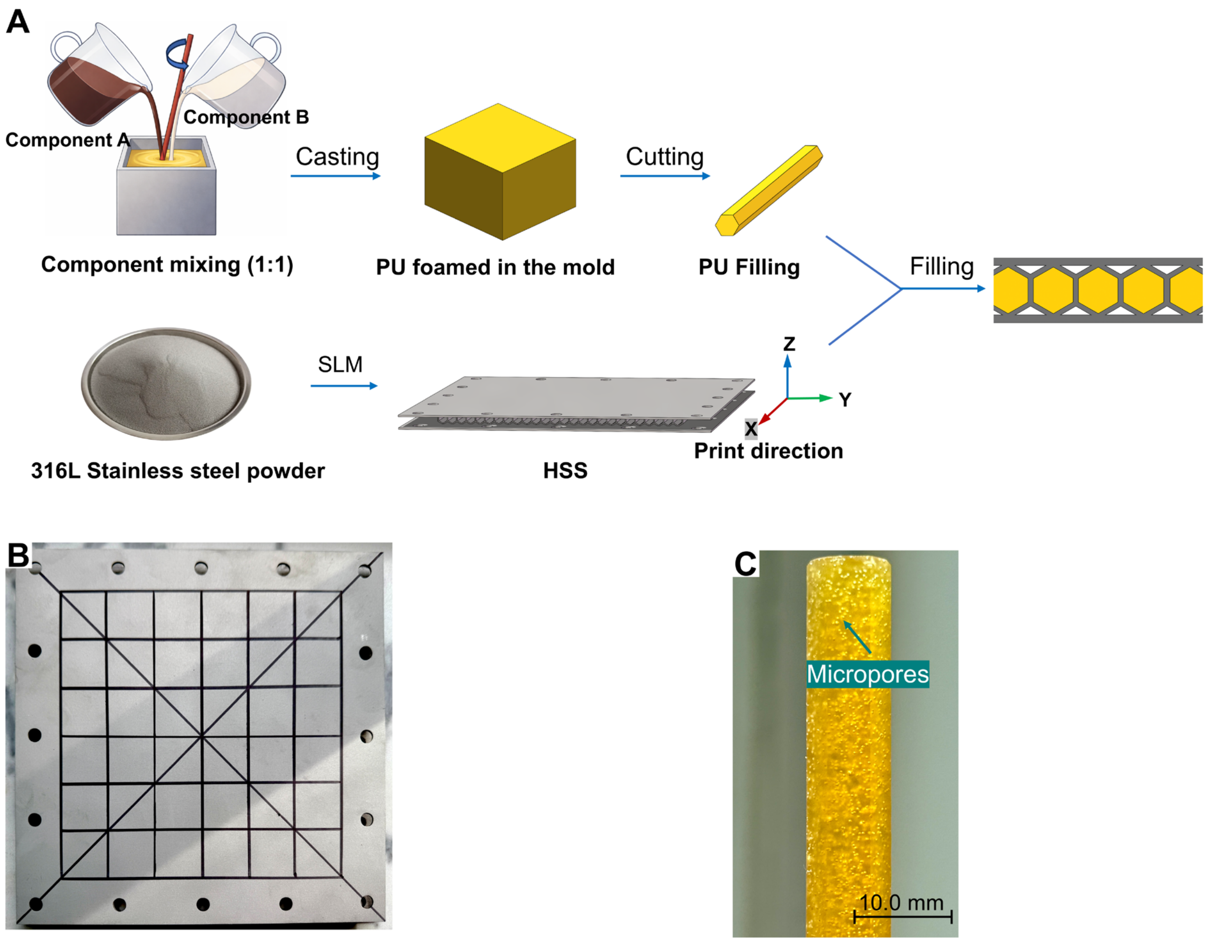

Figure 2. Fabrication procedure: (A) Schematic illustration of the fabrication procedure; (B) SLM-fabricated 316L stainless steel honeycomb structure; and (C) optical image of the PU specimen
Abbreviations: HSS: Honeycomb sandwich structure; PU: Polyurethane; SLM: Selective laser melting.

To quantify the post-blast deformation, each specimen's front and back surfaces were scanned with a G5-630 3D laser scanner (Guangzhou Shanchuang 3D Technology Co., Ltd., China) for geometry reconstruction. Residual deflection profiles along the blast centerline were extracted for both the front and back surfaces. The blast centerline direction is perpendicular to the honeycomb cell cross-section. Finally, each specimen was sectioned along the blast centerline for analyzing internal structural deformation.

2.3. Mechanical tests of SLM 316L stainless steel

2.3.1. Quasi-static and high-strain-rate mechanical testing

To obtain experimentally calibrated material parameters for the subsequent numerical simulations, the mechanical properties of SLM 316L stainless steel along the build direction were characterized through quasi-static tensile tests, room-temperature high-strain-rate compression tests, and elevated-temperature high-strain-rate compression tests.

The specimens used for the basic mechanical tests were fabricated using the same SLM processing parameters and post-processing heat treatment as the honeycomb sandwich specimens and were subsequently machined into the required geometries for quasi-static tensile and dynamic compression tests.

The quasi-static tensile specimen and its detailed dimensions are shown in Figure 4A. The quasi-static tensile tests were conducted at a strain rate of 0.001 s^{-1} using a universal testing machine, as shown in Figure 4B. The engineering stress–strain curves obtained from the quasi-static tensile tests are provided in Figure A1. For the dynamic compression tests, cylindrical specimens were

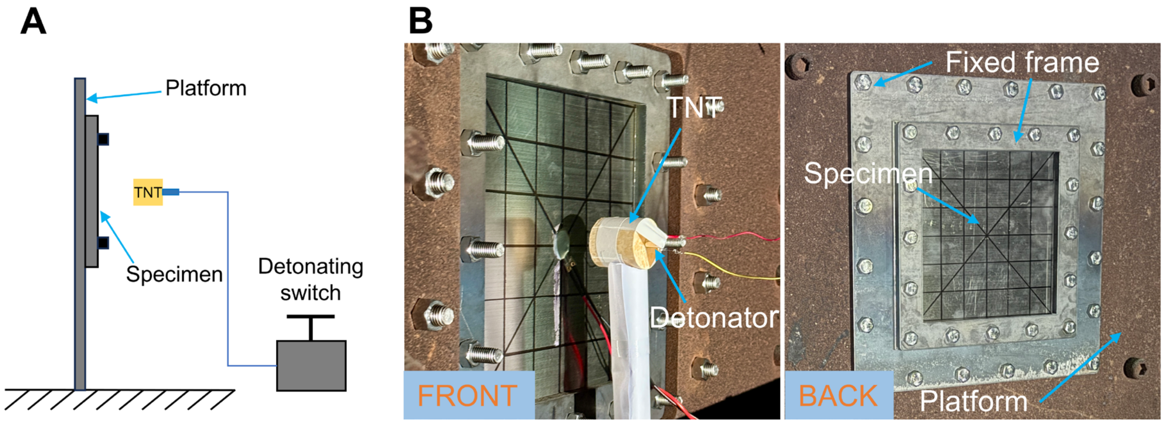

Figure 3. Experimental setup for the near-field explosion tests: (A) Schematic of the experimental setup; (B) front and back photographs of the specimen Abbreviation: TNT: Trinitrotoluene.

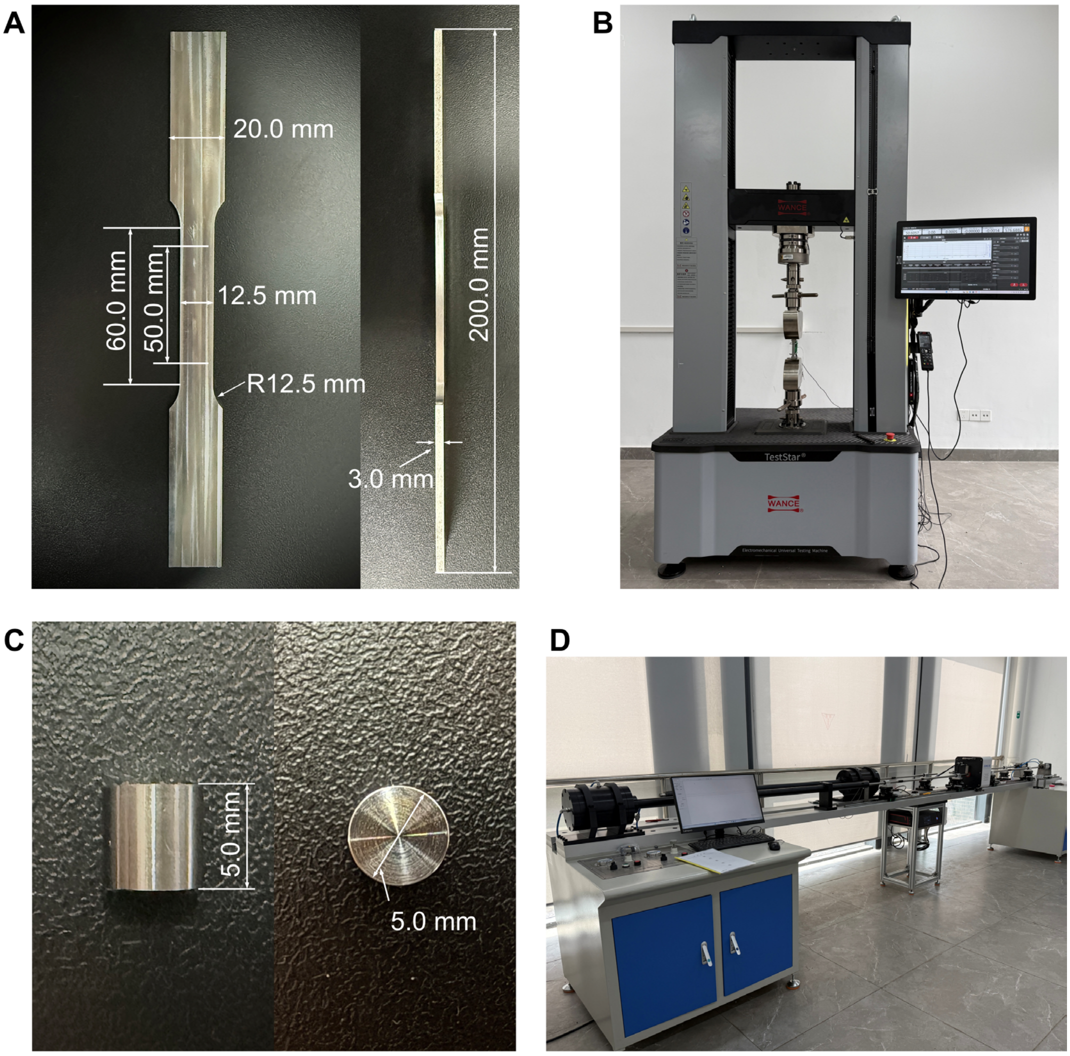

Figure 4. Basic mechanical testing of SLM 316L stainless steel: (A) Tensile specimen; (B) quasi-static tensile testing system; (C) cylindrical specimen for dynamic compression tests; and (D) split Hopkinson pressure bar system

used, as shown in Figure 4C. Room-temperature high-strain-rate compression tests were performed using a split Hopkinson pressure bar system, as shown in Figure 4D. Different strain-rate loading conditions were obtained by adjusting the incident gas pressure to 0.1 MPa, 0.2 MPa, and 0.3 MPa, respectively. Elevated-temperature high-strain-rate compression tests were conducted using a heating furnace attached to the split Hopkinson pressure bar system. The tests were performed at 200 °C and 400 °C under an incident gas pressure of 0.1 MPa. For each testing condition, three repeated tests were conducted to ensure the reliability of the experimental results.

2.3.2. Calibration of Johnson–Cook constitutive parameters

The strain-rate- and temperature-dependent plastic behavior of the SLM 316L stainless steel was described using the Johnson–Cook constitutive model. The flow stress is expressed as follows:

$$\sigma=\left(A+B\varepsilon_{p}^{n}\right)\left[1+C\ln\left(\frac{\dot{\varepsilon}_{p}}{\dot{\varepsilon}_{0}}\right)\right]\left[1-\left(\frac{T-T_{r}}{T_{m}-T_{r}}\right)^{m}\right] \tag{1}$$

where σ is the equivalent flow stress, ε_p is the equivalent plastic strain, $\dot{\varepsilon}_p$ is the equivalent plastic strain rate, and $\dot{\varepsilon}_0$ is the reference strain rate. A, B, and n represent the initial yield stress, strain-hardening coefficient, and strain-hardening exponent, respectively; C is the strain-rate sensitivity coefficient, and m is the thermal-softening exponent. T, Tr, and Tm are the current material temperature, room temperature, and melting temperature, respectively.

The Johnson–Cook constitutive parameters were calibrated based on the quasi-static tensile tests, room-temperature split Hopkinson pressure bar (SHPB) compression tests, and elevated-temperature SHPB compression tests. The overall experimental calibration procedure is shown in Figure 5. The initial yield stress parameter A was determined using the 0.2% offset method, and the average yield stress from three repeated tensile tests was taken as A = 353.3 MPa. After yielding, the plastic strain of each curve was shifted to zero at the corresponding yield point, and the uniform plastic deformation stage was selected for strain-hardening calibration. With A fixed, the parameters B and n were obtained by nonlinear least-squares fitting using all valid data points from the three tensile curves. As shown in Figure 5A, the fitted strain-hardening curve agrees well with the experimental data, giving B = 1,067.4 MPa and n = 0.684, with a coefficient of determination of R^2 = 0.978.

The strain-rate hardening coefficient C was calibrated using the room-temperature SHPB compression results. For each impact pressure, the relatively stable and common true plastic strain interval of 0.02–0.10 was selected. The strain rate was first averaged within this interval for each specimen and then averaged among repeated tests under the same impact pressure. The representative strain rates corresponding to impact pressures of 0.1, 0.2, and 0.3 MPa were 1,584, 3,147, and 3,980 s^{-1}, respectively. Based on the previously determined quasi-static strain-hardening parameters and using the reference strain rate $\dot{\varepsilon}_0$ = 1.0 × 10^{-3} s^{-1}, C was obtained by least-squares fitting of the normalized flow stress. As shown in Figure 5B, the flow stress increases with increasing strain rate, and the fitted strain-rate hardening coefficient was C = 0.0526.

The thermal-softening exponent m was further determined from the elevated-temperature SHPB compression tests conducted at 200 and 400 °C under an impact pressure of 0.1 MPa. For each temperature, three repeated tests were interpolated and averaged pointwise within the common true plastic strain interval of 0.02–0.10. The complete Johnson–Cook model was then used with T_r = 24 °C and T_m = 1,400 °C, while the previously calibrated parameters A, B, n, and C were kept fixed. As shown in Figure 5C, the flow stress decreases substantially with increasing temperature, indicating the thermal softening behavior of SLM 316L stainless steel. The exponent m was obtained by least-squares fitting of the thermal-softening term, giving m = 1.4628.

2.4. Numerical model

2.4.1. S-ALE model

A numerical model of the dynamic response of the PU-filled 316L stainless steel HSS under blast loading was developed using the S-ALE algorithm in the commercial finite-element code LS-DYNA, as shown in Figure 6. A one-quarter symmetric model (1/4 symmetry) was used. The model describes the entire process from charge detonation to HSS response to structural energy absorption.

The detailed geometry of the clamping fixture was not explicitly modeled. Instead, the blast-effective region corresponding to the experiments was modeled, and the plate edges were fully constrained to represent the clamped boundary condition. For the air domain, dimensions of 60 mm × 60 mm × 150 mm were used for the 50 mm and 75 mm stand-off cases, and 60 mm × 60 mm × 200 mm for the 100 mm stand-off case.

In the geometric model, the HSS was represented as solids using the LS-DYNA solid element type 164 and placed in the Lagrangian domain. The air domain and the explosive after detonation were treated as fluids and therefore modeled with Eulerian formulations. The cylindrical charge (Φ35 mm × 35 mm) was defined

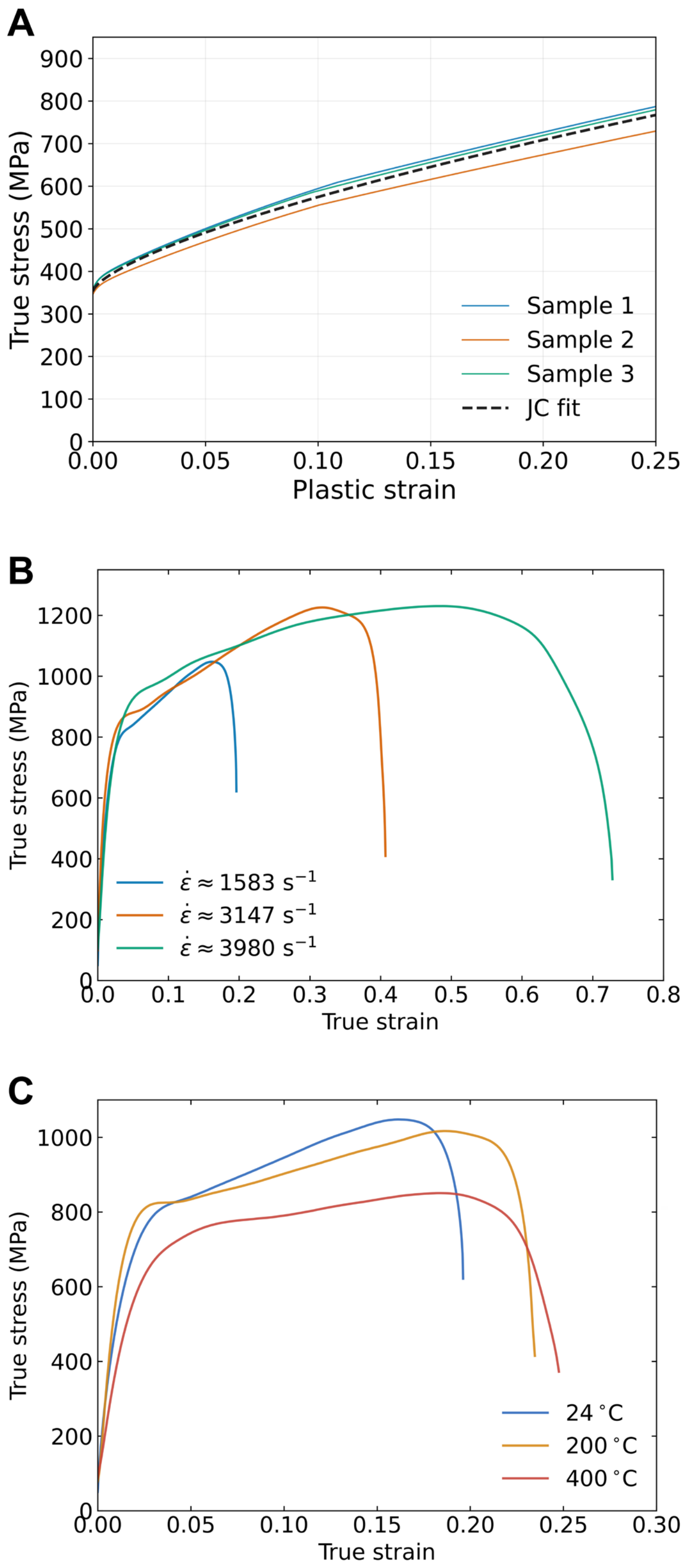

Figure 5. Experimental calibration procedure of the Johnson–Cook constitutive model for SLM 316L stainless steel: (A) Quasi-static tensile response and strain-hardening fit, (B) averaged dynamic compressive responses at different strain rates, and (C) averaged temperature-dependent dynamic compressive responses at an impact pressure of 0.1 MPa

using *INITIAL_VOLUME_FRACTION_GEOMETRY (volume-filling method).

All six degrees of freedom of the HSS boundary nodes were fully constrained at the plate edges. Symmetry boundary conditions were applied on the XY and YZ symmetry planes. Non-reflecting boundary conditions (*BOUNDARY_NON_REFLECTING) were used on the air domain boundaries to simulate free outflow of detonation products.

To prevent penetration and other nonphysical behavior during large deformation, contact definitions were specified between the different components of the HSS. The contact between the honeycomb cell walls and the face sheets was modeled using *CONTACT_ERODING_SURFACE_TO_SURFACE. The self-contact of the honeycomb walls was defined using *CONTACT_ERODING_SINGLE_SURFACE. The contact between the PU filling and the metallic honeycomb walls was also modeled using *CONTACT_ERODING_SURFACE_TO_SURFACE, and the interior contact of the PU was defined using *CONTACT_INTERIOR. All contact formulations were based on penalty algorithms and were applied consistently over the entire HSS region.

To determine an appropriate air mesh size, three element sizes (0.5 mm, 0.75 mm, and 1.0 mm) were tested. Pressure histories were extracted from air elements located 1.5 mm above the center of the front surface. The resulting pressure–time traces are shown in Figure 7. Two characteristic pressure peaks were identified on each curve: the first peak corresponds to the incident pressure, while the subsequent larger peak corresponds to the reflected pressure produced by the interaction of the blast wave with the HSS surface. At approximately 150 μs, the pressure has nearly recovered to the initial ambient level, indicating that the fluid–structure interaction stage is almost complete. The 0.5 mm and 0.75 mm meshes yielded comparable reflected pressure responses, whereas the 1.0 mm mesh exhibited slightly lower peak values. Since the reflected pressure has a greater influence on the overall structural response, it was used as the main criterion for mesh convergence evaluation. The reflected peak pressures obtained with different mesh sizes at the stand-off distance of 50 mm, along with the relative deviation referenced to the 0.75 mm mesh, are summarized in Table 1. The results for the 0.75 mm mesh at stand-off distances of 75 mm and 100 mm are also included for comparison. Therefore, balancing accuracy and computational efficiency, a 0.75 mm mesh was selected for the subsequent numerical model.

2.4.2. Material models

(a) 316L stainless steel

The 316L stainless steel used as the main structural material of the HSS was modeled using *MAT_JOHNSON_COOK in LS-DYNA, together with the equation of state *EOS_GRUNEISEN. The Johnson–Cook parameters calibrated in Section 2.3.2 were directly adopted in the numerical model, ensuring consistency between the material characterization and blast simulations. The equation of state *EOS_GRUNEISEN is used to describe the pressure of compressible materials. The specific form of the pressure definition is as follows:

$$P = \frac{\rho_0 C_0^2 \mu \left[1 + \left(1 - \frac{\gamma_0}{2} \right) \mu - \frac{\alpha}{2} \mu^2 \right]}{1 - \left(S_1 - 1 \right) \mu - S_2 \frac{\mu^2}{\mu + 1} - S_3 \frac{\mu^3}{\left(\mu + 1 \right)^2}} + \left(\gamma_0 + \alpha \mu \right) E \tag{2}$$

where E is the internal energy per initial volume, C_0 is the intercept of the v_s–v_p curve, which represents the bulk

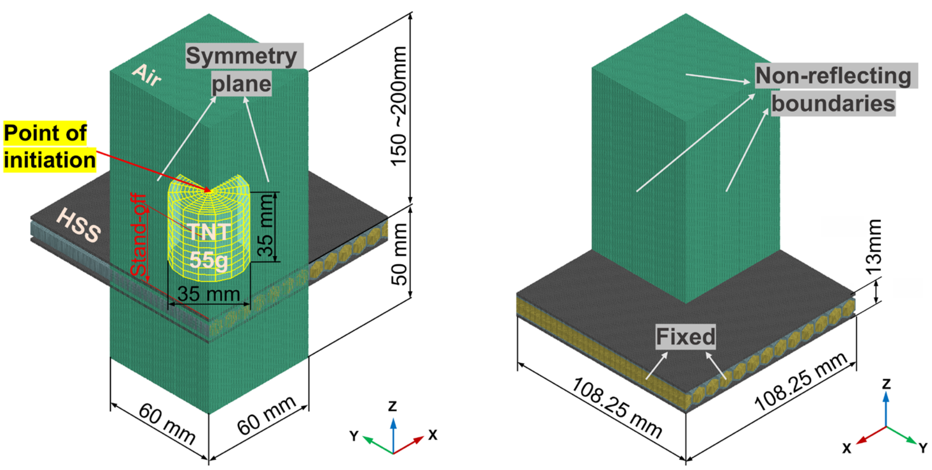

Figure 6. Schematic of the S-ALE model geometric configuration and boundary settings

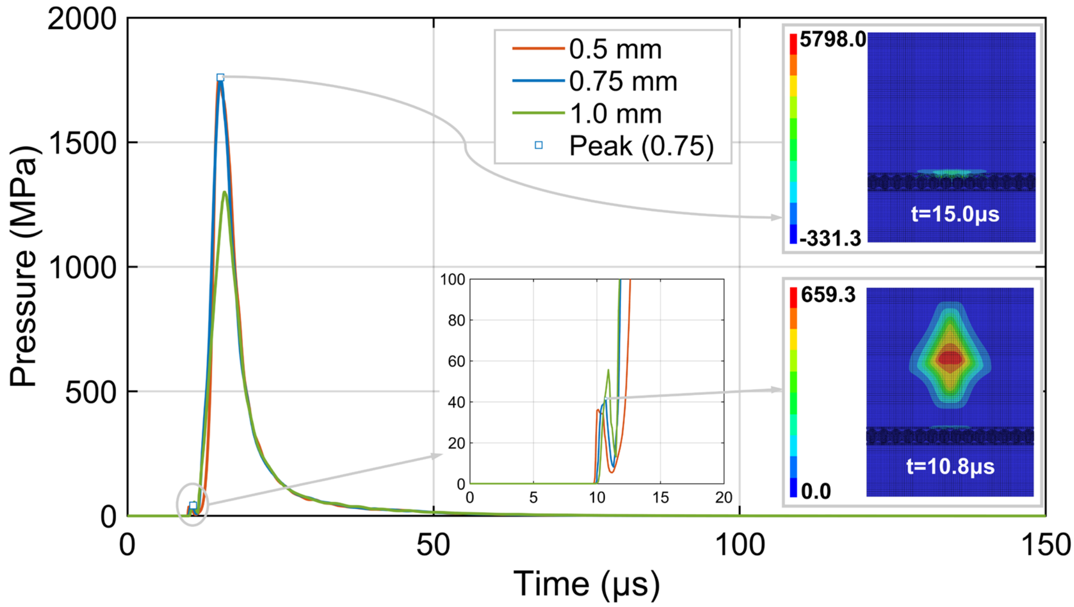

Figure 7. Pressure–time history extracted 1.5 mm in front of the front-surface center at a stand-off distance of 50 mm, together with pressure contours at the corresponding times

speed of sound. S_1, S_2, and S_3 are coefficients for the slope of the v_s–v_p curve, γ_0 is the Gruneisen constant, $\mu = \rho/\rho_0 - 1$, where ρ_0 and ρ are the initial and current material densities, respectively. α is the first-order volume correction coefficient for γ_0. The specific values of the aforementioned parameters are given in Table 2.

Table 1. Effect of mesh size on reflected peak pressures

Stand-off/mm	Z (m·kg$^{-1/3}$)	Mesh size/ mm	Reflected peak pressure (MPa)	Relative deviation (%)
		0.50	1,771.1	0.8
50	0.1315	0.75	1,757.2	0.0
		1.00	1,297.1	−26.2
75	0.1972	0.75	1,131.9	–
100	0.2630	0.75	762.8	–

(b) Air

In the numerical model, air was treated as an ideal gas, defined using the constitutive material model *MAT_NULL, and the equation of state *EOS_LINEAR_POLYNOMIAL was selected.

$$P = C_1 + C_2\mu + C_3\mu^3 + \left(C_4 + C_5\mu + C_6\mu^2\right)E_i \tag{3}$$

In **Equation 3**, P is the air pressure, $\mu = \rho/\rho_0 - 1$, $C_1 = C_2 = C_3 = C_6 = 0$, $C_4 = C_5 = \gamma - 1$. γ is the specific heat ratio of the gas. E_i is the initial internal energy per unit volume of air, taken as 0.25 MPa.

(c) Trinitrotoluene

Trinitrotoluene explosive was defined and described using the *MAT_HIGH_EXPLOSIVE_BURN model, and the equation of state *EOS_JWL was selected, expressed as follows:

$$P = a\left(1 - \frac{\omega\rho}{R_1\rho_0}\right)e^{-\frac{R_1\rho_0}{\rho}} + b\left(1 - \frac{\omega\rho}{R_2\rho_0}\right)e^{-\frac{R_2\rho_0}{\rho}} + \omega\rho E \tag{4}$$

In **Equation 4**, P is the detonation pressure, ρ_0 is the density of the detonation products, ρ is the density of the explosive itself, E is the internal energy per unit mass of the explosive, and a, b, R_1, R_2, and ω are characteristic parameters of the explosive. The material model parameters and equation of state parameters used in this study are listed in Table 2.

(d) Polyurethane

The *MAT_CRUSHABLE_FOAM model was selected to describe the PU. This model is used to represent crushable foams with damping. The unloading process is fully elastic, and the transition at the stress cutoff is defined from elastic to fully plastic behavior. Its parameters: density $\rho = 1.08$ g/cm^3, Poisson's ratio $\nu = 0.2$, and a damping coefficient of 0.5. The PU material behavior was defined based on the experimentally measured uniaxial compression stress–strain curve (Figure A2).

2.4.3. Numerical validation

To validate the accuracy of the numerical model, the residual deflection profiles along the blast centerline were compared between the experimental and simulated results at stand-off distances of 50 mm, 75 mm, and 100 mm, as shown in Figure 8. Overall, the numerical results reproduce the main deformation characteristics observed in the experiments, including the peak position near the blast center, the symmetric deflection profile along the centerline, and the decreasing residual deflection with increasing stand-off distance. Although the simulation slightly overestimates the central deflection at the 50 mm stand-off distance, the predicted curves show acceptable agreement with the experimental profiles for all three loading conditions.

Furthermore, the maximum residual deflections along the blast centerline were quantitatively compared, as summarized in Table 3. The relative errors between the experimental and numerical results are within 14% for all stand-off distances. Considering the inherent scatter of near-field blast experiments, as well as the fact that the Johnson–Cook parameters used in the model were independently calibrated from basic mechanical tests rather than adjusted according to the blast results, the present numerical model can be considered reliable for capturing the dynamic response and deformation trend of the PU-filled HSS under near-field blast loading.

3 Results

3.1. Deformation patterns

Figure 9 presents the front-face morphologies of the HSS and the equal-areal-density solid plate after exposure to near-field blast loading at different stand-off distances. Jacob *et al.*[43] classified the deformation and failure modes of low-carbon steel plates subjected to explosive loading based on the degree of load localization and target response characteristics. These modes include: Mode I, large plastic deformation; Mode II, tensile tearing at the boundary; Mode III, transverse shear failure at the boundary; Mode II*c, localized tearing in the central region; Mode II c, complete tearing in the central region; and Petalling, petal-shaped tearing.

In this study, both the HSS and solid plate exhibited typical Mode I localized plastic deformation characteristics, with damage mainly concentrated in the region near the projection of the explosion center. For the HSS, the front face sheet experienced localized indentation under blast impact because the cell openings provided nonuniform support between adjacent honeycomb walls. Additionally, several erosion pits were observed on the front surfaces of both specimen types, as highlighted in the magnified inset circles.

Figure 10 shows the back-face morphologies of the HSS and the equal-areal-density solid plate after exposure to near-field blast loading at different stand-off distances. No obvious damage was observed on the back surfaces of any specimen, and the degree of bending deformation

Table 2. Parameters of the material constitutive model and equation of state used in this simulation[41,42]

Material	Parameters				
316L stainless steel	ρ (g·cm^{-3})	E (GPa)	v	A (MPa)	B (MPa)
	7.95	195	0.25	353.3	1,067.4
	T_r (K)	T_m (K)	n	C	$\dot{\varepsilon}_0\left(s^{-1}\right)$
	297	1,673	0.684	0.0526	1.0×10^{-3}
	C_0 (m·s^{-1})	S_1	S_2, S_3	γ_0	α
	4,578	1.36	0	1.67	0.45
Trinitrotoluene	ρ (g·cm^{-3})	V_D (m·s^{-1})	P_{CJ} (GPa)	a (GPa)	b (GPa)
	1.63	6930	21	373.8	3.75
	R_1	R_2	ω		
	4.15	0.9	0.35		

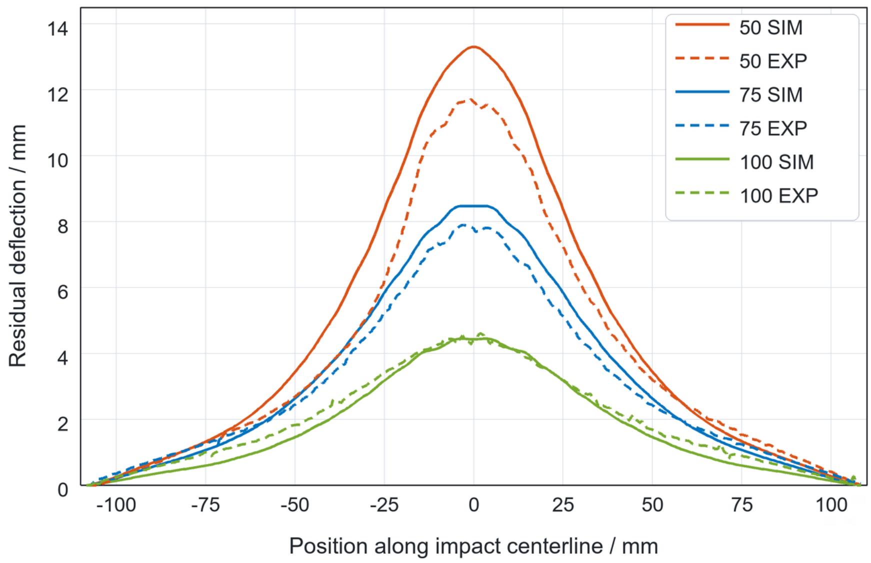

Figure 8. Experimental and numerical residual deflection curves along the blast centerline
Abbreviations: EXP: Experimental result; SIM: Simulation result.

decreased with increasing stand-off distance. At the same distance, the HSS exhibited substantially smaller back-face deformation compared to the solid plate. For the equal-areal-density solid plates at stand-off distances of 50 mm and 75 mm, pronounced overall bending deformation of the back surface was observed.

Table 3. Comparison of experimental and numerical maximum residual deflections along the blast centerline under different stand-off distances

Stand-off distance (mm)	EXP (mm)	SIM (mm)	relative error (%)
50	11.7	13.3	13.7
75	7.9	8.5	7.6
100	4.6	4.4	−4.3

Abbreviations: EXP: Experimental result; SIM: Simulation result.

Figure 11A and 11B illustrate the cross-sectional morphologies of the HSS and the solid plate along the blast centerline under three different stand-off distances. For the HSS, the core layer underwent progressive honeycomb cell collapse, with evident buckling and folding of the cell walls. At the central cells, the front face sheet was severely folded into the core layer, exhibiting pronounced localized plastic deformation. In contrast, the solid plate mainly dissipated energy through global bending deformation, indicating relatively weaker local load dispersion capability.

These morphological comparisons demonstrate that the introduction of the honeycomb core and PU filling enables effective load dispersion and transforms global bending deformation into localized energy absorption through the plastic deformation of the core and the compressive deformation of the filling. Consequently, the structure's blast resistance under a near-field explosion is markedly enhanced, with the PU filling providing excellent structural support.

As the stand-off distance increases from 50 mm to 100 mm, the indentation depth on the HSS front face sheet markedly decreases, and the bending deformation of the solid plate also becomes markedly smaller. This trend indicates that the intensity of the blast wave propagating through the air attenuates rapidly with distance, thereby reducing the loading intensity acting on the structures.

Figure 11C and 11D show the residual deflection profiles, quantitatively reflecting the deformation differences described above. The curves clearly reveal the indentation pattern of the HSS front surface along the blast centerline, as well as the substantially smaller back surface deflection compared to the solid plate at the same stand-off distance. The deflection curve of the solid plate is smooth, whereas that of the HSS exhibits a serrated shape corresponding to the deformation characteristics of its porous core structure.

Table 4 compares the maximum residual deflection

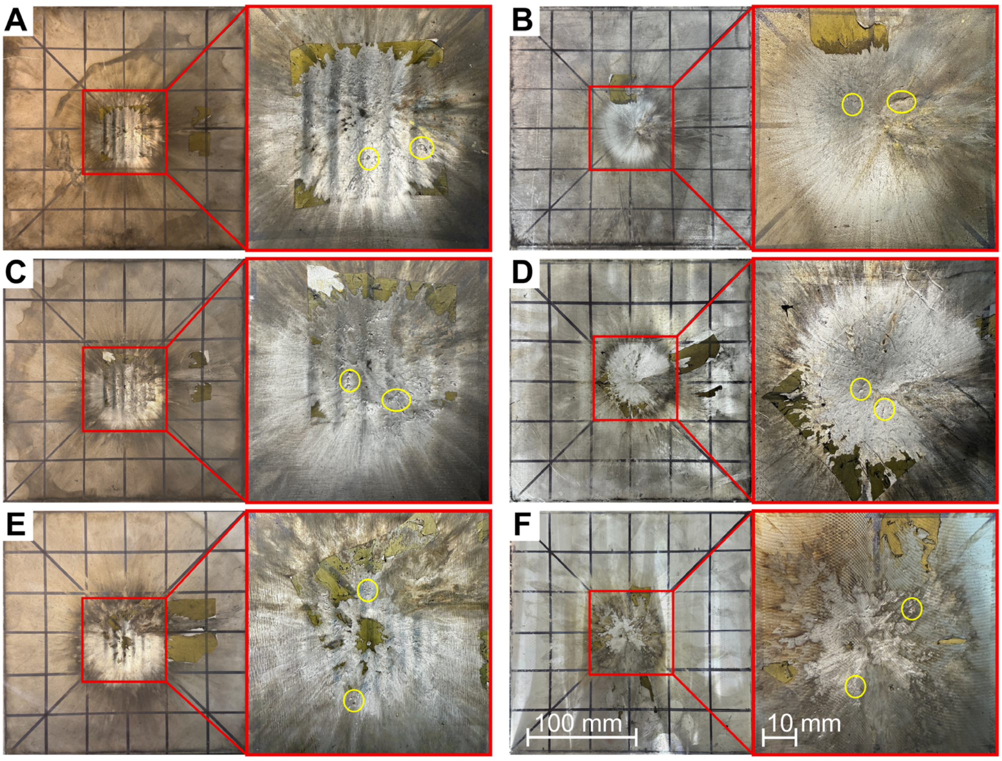

Figure 9. Front surface photographs of six specimens: (A) H50, (B) S50, (C) H75, (D) S75, (E) H100, (F) S100. Scale bars: Left: 100 mm; right: 10 mm.

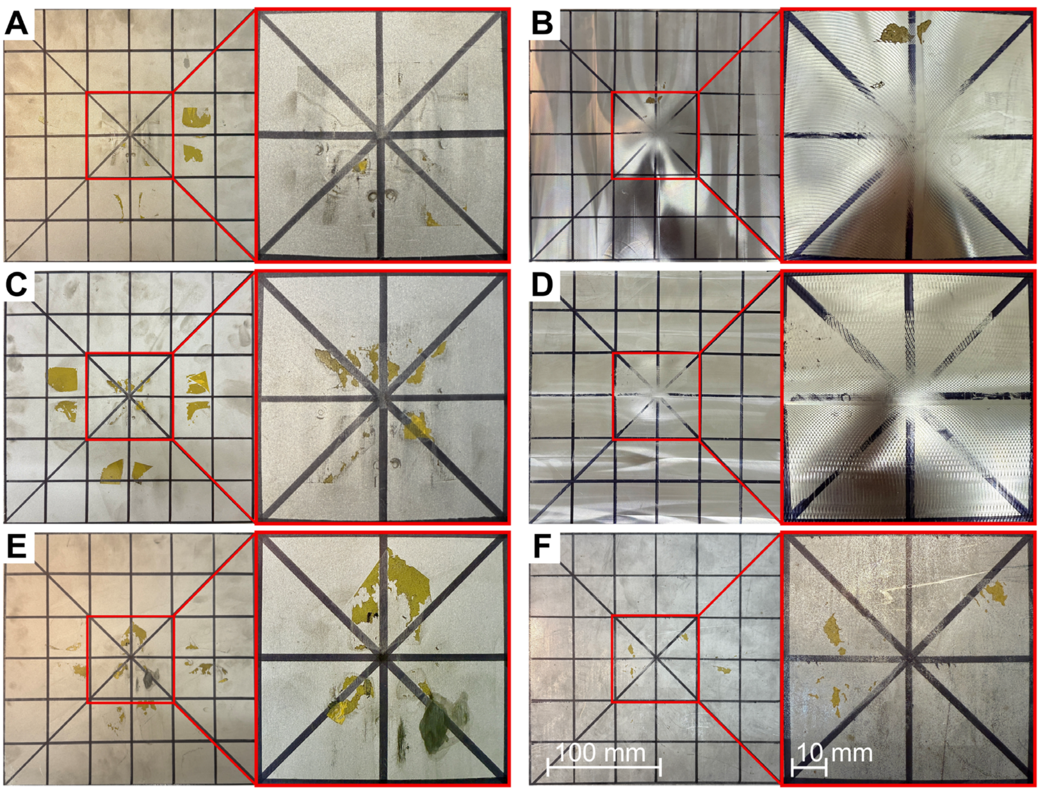

Figure 10. Back surface photographs of six specimens: (A) H50, (B) S50, (C) H75, (D) S75, (E) H100, (F) S100. Scale bars: Left: 100 mm; right: 10 mm.

along the blast centerline between the HSS and the solid plate. At a stand-off distance of 50 mm, the front-face deflection of the HSS is slightly smaller than that of the solid plate, while at 75 mm and 100 mm, the maximum front-face deflection of the HSS becomes slightly larger, indicating a deeper local indentation of the front-face sheet. However, the back-face deflections of the HSS are smaller than those of the solid plate at all stand-off distances.

In particular, at stand-off distances of 50 mm and 100 mm, the residual deflection at the center of the HSS back face is reduced by 20.4% and 19.3%, respectively, compared with the solid plate. This result demonstrates that the honeycomb core and the PU filling effectively attenuate the transmission of impact energy to the back face through compressive deformation. As one of the most critical indicators for evaluating the blast resistance of a structure, the smaller maximum back-face deflection clearly confirms the superior blast-resistant performance of the HSS.

3.2. Structure response

Figure 12 shows the von Mises stress contours of the HSS structure at different stand-off distances and various time instances. The four selected moments correspond to: the instant when the shock wave reaches the front face sheet (t_a), the moment when the front-face center velocity reaches its maximum ($t_{front,max}$), the moment when the back-face center velocity reaches its maximum ($t_{back,max}$), and the moment when the back-face deflection reaches its maximum ($t_{d,max}$).

Table 4. Comparison of the maximum residual deflection at the blast centerline between the honeycomb sandwich structure (HSS) and the solid plate

Stand-off distance (mm)	HSS front (mm)	Solid front (mm)	Change in front-face deflection (%)	HSS back (mm)	Solid back (mm)	Reduction back (%)
50	14.7	15.3	3.9	11.7	14.7	20.4
75	10.4	9.3	−11.8	7.9	9.1	13.2
100	6.3	5.6	−12.5	4.6	5.7	19.3

Note: Negative values indicate a larger deflection of the HSS relative to the solid plate.

At $t_{front,max}$ under the 50 mm stand-off distance, the central region of the structure exhibits extremely high stress

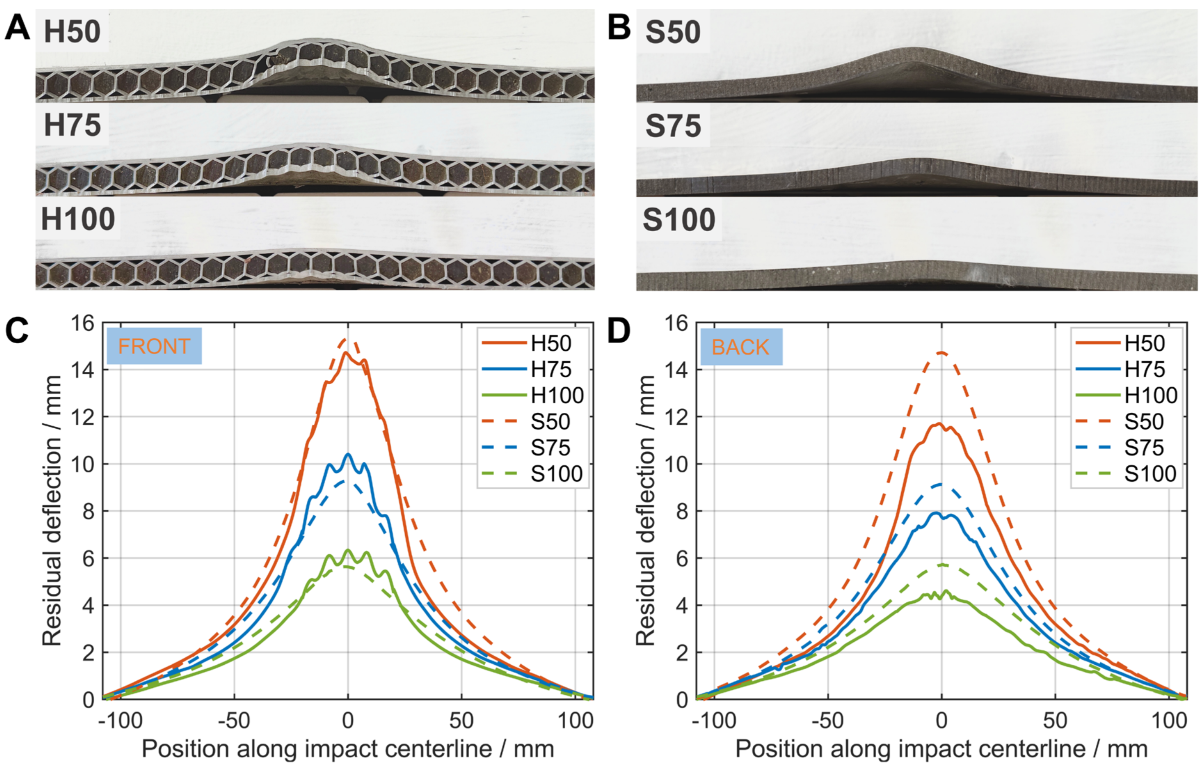

Figure 11. Deflection of the specimens: (A) Cross-sectional photographs of honeycomb sandwich structure specimens, (B) cross-sectional photographs of solid specimens, (C) front surface residual deflection of six specimens, and (D) back surface residual deflection of six specimens

levels, with the front face sheet and the honeycomb walls near the explosion center entering the plastic state, showing pronounced stress concentration. As the stand-off distance increases, the extent of the high-stress region decreases, and the peak stress values are substantially reduced. The stress distribution indicates that the honeycomb core plays a crucial role in load transmission, effectively dissipating the impact energy through its plastic deformation and progressive failure mechanisms.

To gain deeper insight into the dynamic response of the structure, the velocity–time histories at the centers of the front and back face sheets of the HSS under different stand-off distances were extracted from the numerical simulations, as shown in Figure 13. The corresponding maximum velocities and their occurrence times are summarized in Table 5.

Table 5. Maximum velocities and corresponding times of the front and back faces

Stand-off distance (mm)	$v_{front,max}$ (m/s)	$t_{front,max}$ (μs)	$v_{back,max}$ (m/s)	$t_{back,max}$ (μs)
50	584.8	15.0	251.3	32.2
75	443.6	21.2	184.7	45.2
100	332.3	27.2	97.8	47.2

At a stand-off distance of 50 mm, the front-face center reaches a maximum velocity of 584.8 m/s at approximately 15.0 μs after detonation, indicating an intense initial response of the front-face sheet upon blast-wave loading. In comparison, the maximum velocity at the back-face

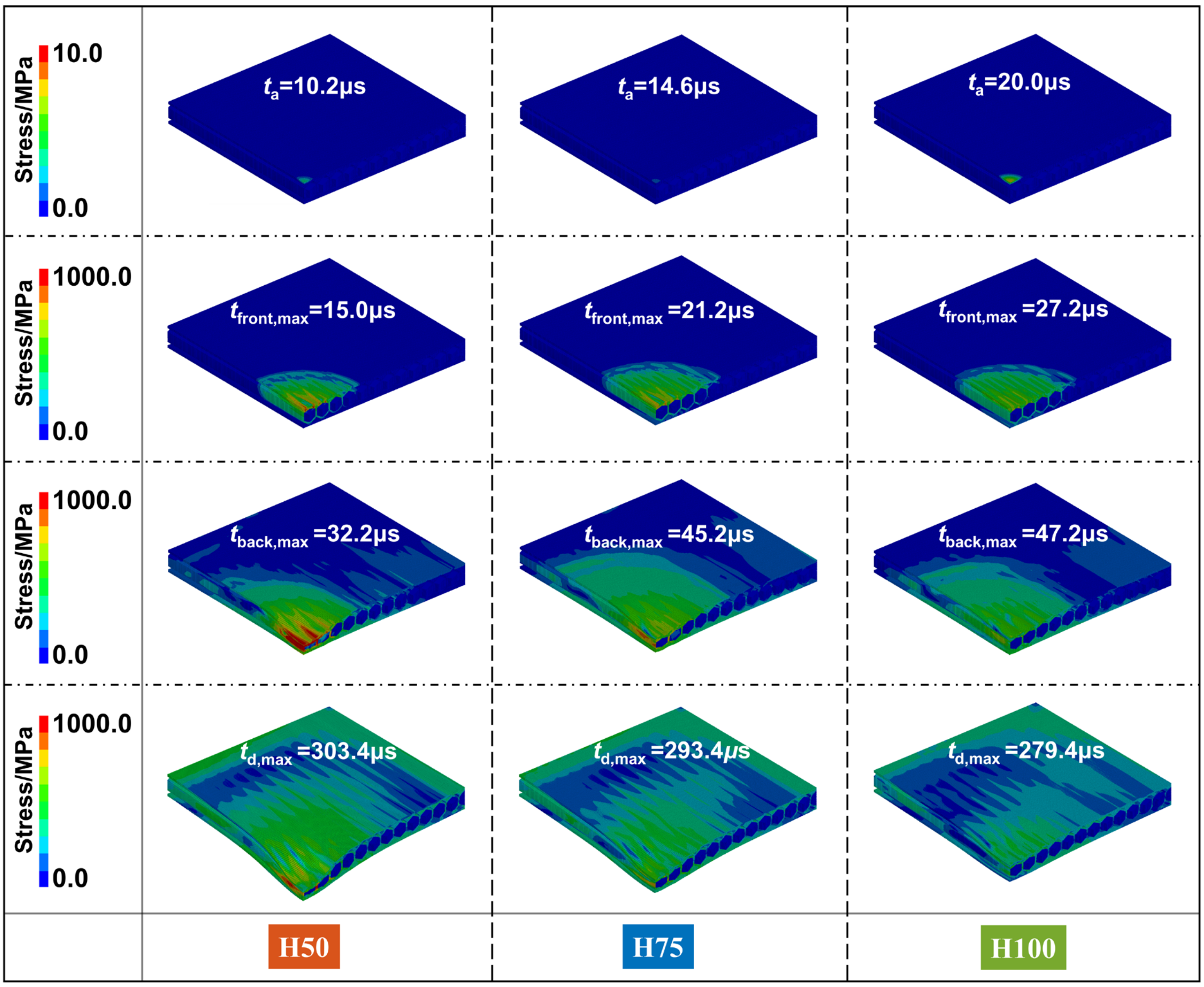

Figure 12. Von Mises stress contours of honeycomb sandwich structure specimens under three stand-off distances: H50, H75, and H100

center is substantially lower, reaching 251.3 m/s at 32.2 μs. The reduced magnitude and delayed occurrence of the back-face peak indicate that the blast-induced load is effectively attenuated and temporally dispersed during its transfer through the PU-filled honeycomb core.

As the stand-off distance increases from 50 mm to 75 and 100 mm, the maximum front-face velocity decreases by 24.1% and 43.2%, respectively, while its occurrence time is delayed by 41.2% and 81.2%. Similarly, the maximum back-face velocity decreases by 26.5% and 61.1%, respectively, accompanied by increases of 40.4% and 46.6% in its occurrence time. These results demonstrate that increasing the stand-off distance reduces the blast-load intensity and delays the arrival of the peak structural response. Moreover, the consistently lower and later-occurring velocity peaks at the back face further confirm the significant load-attenuation capability of the metallic honeycomb–PU composite core.

3.3. Energy absorption characteristics

The internal energy of each component, including the front face sheet, honeycomb core, PU filling, and back face sheet, was extracted to characterize its respective deformation energy absorption. To quantify the contribution of each component during the blast-resistance process, the internal energy histories under the three stand-off distances are compared in Figure 14A. At approximately 600 μs, the energy absorption of all components became stable. The corresponding absorbed energies and proportions at this time are summarized in Figure 14B.

The energy–time histories indicate that the honeycomb core was the primary energy-absorbing component under all three stand-off distances, accounting for 44.6–46.3% of the total absorbed energy. It also approached saturation later than the other components, whereas the PU filling exhibited rapid energy absorption during the early loading stage. The back face sheet showed delayed and substantially lower energy absorption than the front face sheet, contributing only 6.9–8.2% of the total absorbed energy. As the stand-off distance increased from 50 to 100 mm, the total absorbed energy decreased markedly from 843.1 to 228.0 J.

At the smallest stand-off distance of 50 mm, the total absorbed energy of the HSS reached 843.1 J. The honeycomb core absorbed the largest amount of energy, contributing 385.5 J (45.7%), primarily owing to its extensive plastic deformation under the blast load. The front face sheet absorbed 196.6 J (23.3%) through stretching, bending, and localized plastic indentation. The PU filling absorbed 191.7 J (22.7%), mainly through microcell collapse, polymer-matrix deformation, and internal friction. The back face sheet absorbed the least energy, with a contribution of 69.3 J (8.2%), indicating that most of the energy transmitted through the core and filling had been dissipated before reaching the rear surface.

Comparing the mass proportions of the components—23.2% for the front face sheet, 41.2% for the honeycomb core, 12.3% for the PU filling, and 23.2% for the back face sheet—with their corresponding energy absorption ratios further demonstrates the effectiveness

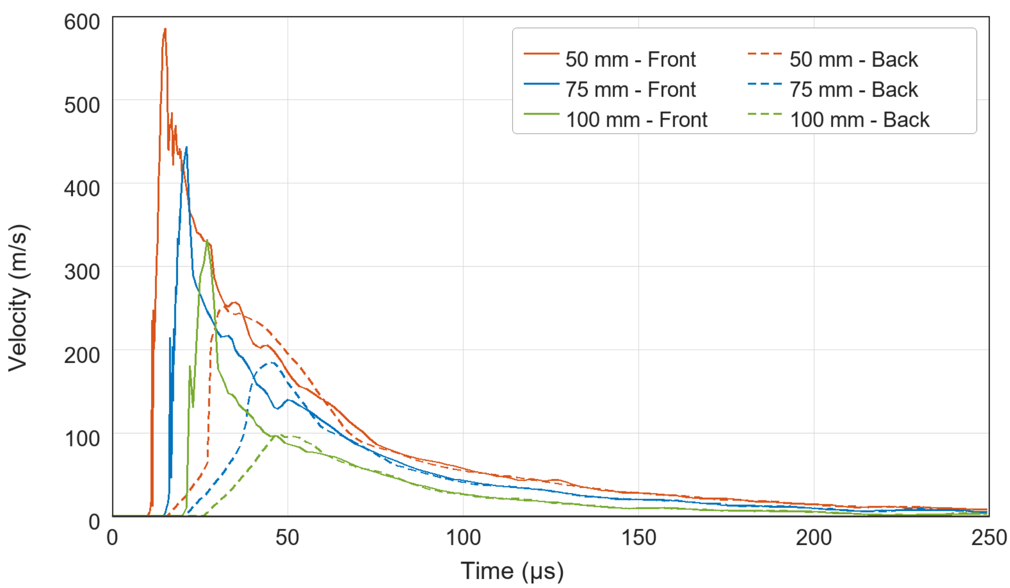

Figure 13. Velocity–time histories at the centers of the front and back face sheets under different stand-off distances

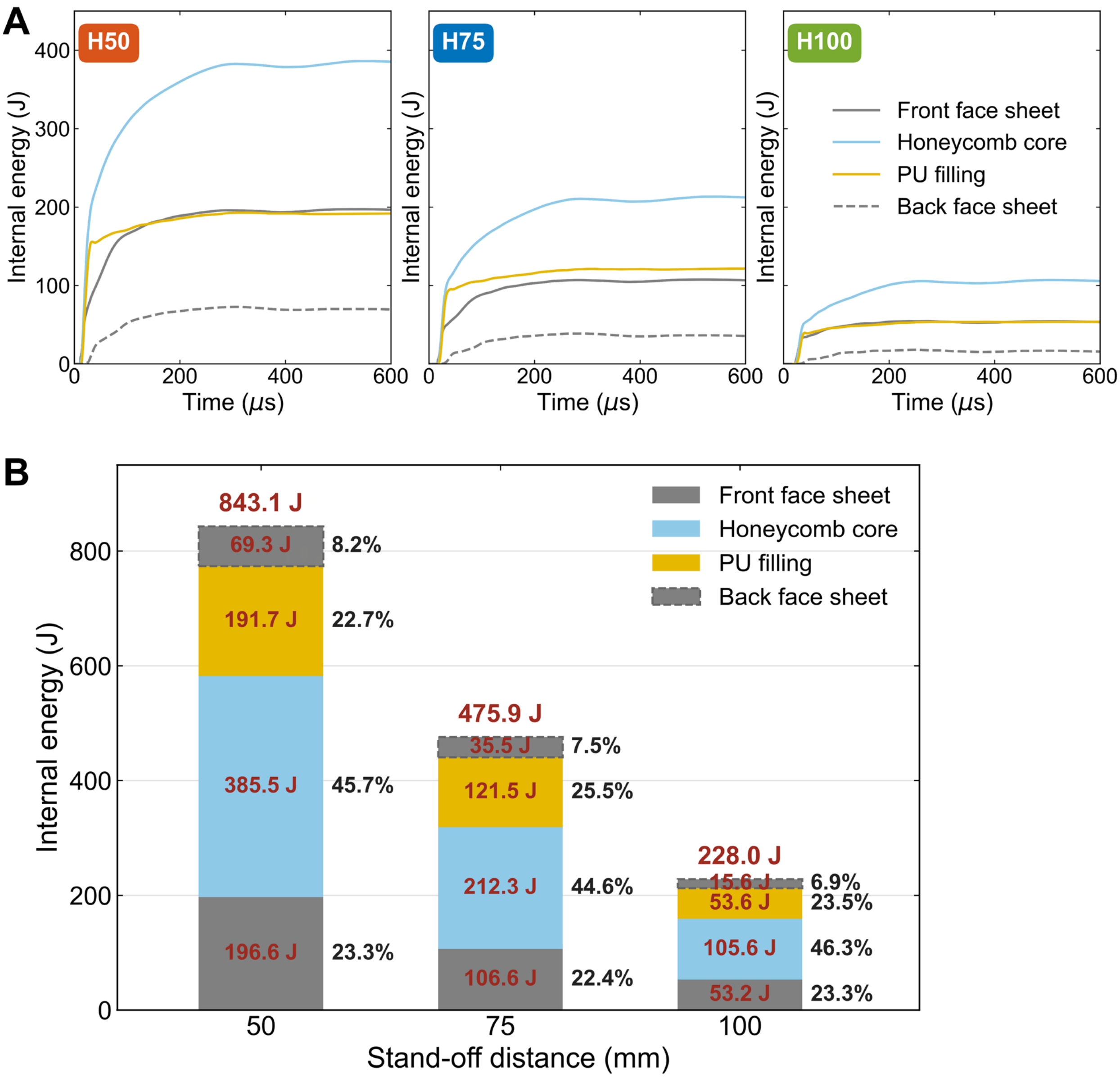

Figure 14. Internal energy absorption of each component in the HSS specimens under different stand-off distances: (A) Time histories of internal energy of each component in the HSS specimens under different stand-off distances, (B) internal energy absorption and proportion of each component at 600 μs under three stand-off distances

Abbreviations: HSS: Honeycomb sandwich structure; PU: Polyurethane.

of the PU filling. Despite accounting for only 12.3% of the total mass, the PU filling contributed 22.7–25.5% of the total absorbed energy, indicating excellent specific energy absorption performance. The honeycomb core also exhibited an energy absorption contribution of 44.6–46.3%, moderately exceeding its mass proportion, whereas the back face sheet contributed substantially less energy than its mass proportion.

4 Discussion

4.1. Reflected peak pressure

The pressure–time histories extracted in this study indicate that the reflected pressures at the scaled distances of Z = 0.1315, 0.1972, and 0.2630 m·kg$^{-1/3}$ were 1757.2, 1131.9, and 762.8 MPa, respectively. In comparison, the empirical predictions based on Shin *et al*.'s[37] spherical charge model yielded reflected pressures of 917.5 MPa, 293.0 MPa, and 130.5 MPa, corresponding to ratios of 1.92, 3.86, and 5.85, respectively. Previous studies have shown that, under identical central initiation conditions, the near-field peak overpressure estimated using a spherical charge may underestimate that of a cylindrical charge by up to a factor of 3.0 at Z = 0.25 m·kg$^{-1/3}$. Moreover, at Z = 0.7 m·kg$^{-1/3}$, the pressure on the initiation side of a single-end-initiated cylindrical charge was found to be approximately 2.5 times higher than that on the opposite side.[39] In the present study, the TNT charge had a length-to-diameter ratio of 1.0 and was initiated at the far end. Compared with the centrally initiated spherical charge, this configuration produced substantially higher reflected pressures in the near-field region. Under such extremely close-in detonation conditions, the characterization of blast loads becomes highly complex, as it is strongly influenced by multiple factors, including detonation products, charge geometry, and initiation configuration.

4.2. Selective laser melting of 316L stainless steel

The mechanical properties of SLM-fabricated 316L stainless steel are closely related to both the printing process and subsequent post-processing treatment. Process parameters such as build orientation, laser power, scanning speed, hatch spacing, and layer thickness collectively determine the energy input per unit volume, thereby governing melt pool stability, densification level, and microstructural characteristics. For example, laser power and scanning speed directly affect the thermal field and cooling rate of the melt pool, while hatch spacing and layer thickness influence inter-layer bonding quality and the formation of porosity.[44] In addition, post-processing heat treatment may further modify the residual stress state and microstructural features of the printed material, thereby affecting its mechanical response. Therefore, different combinations of processing and post-processing conditions generally involve trade-offs among strength, hardness, ductility, and structural integrity, and an optimal parameter set is typically defined with respect to specific performance objectives. Existing studies have shown that, within reasonable processing windows, SLM-fabricated 316L stainless steel can exhibit a dense microstructure with typical melt pool morphology and relatively stable mechanical performance.[24]

A typical feature of SLM-fabricated 316L stainless steel is the direction-dependent mechanical response caused by its layer-wise manufacturing process. The repeated melting and rapid solidification during SLM produce melt-pool boundaries, cellular substructures, crystallographic texture, and columnar grain growth associated with the build direction. These microstructural characteristics may result in differences in yield strength, strain hardening, ductility, and failure behavior between the build direction and the build plane. Therefore, the mechanical response of SLM 316L stainless steel cannot be regarded as completely identical in all loading directions, especially under large deformation and high-strain-rate loading conditions.

In the present study, the material behavior in the numerical simulations was described using an isotropic Johnson–Cook constitutive model. This model was adopted because it provides an effective phenomenological description of strain hardening, strain-rate hardening, and thermal softening and is widely used for high-strain-rate simulations involving large plastic deformation. In order to improve the reliability of the material description, the Johnson–Cook parameters were calibrated from basic mechanical tests of SLM-fabricated 316L stainless steel produced using the same processing route as the HSS specimens, rather than being directly taken from the literature.

Nevertheless, the use of a single-direction, isotropic Johnson–Cook calibration inevitably introduces certain simplifications. The blast response of the HSS involves a complex combination of bending, compression, shear, local buckling, and multiaxial stress states. In addition, the metallic honeycomb walls may experience both tensile-dominated and compressive-dominated deformation during collapse, while SLM-fabricated 316L stainless steel may exhibit anisotropy and tension–compression asymmetry. These effects cannot be fully captured by the present isotropic Johnson–Cook model. This simplification may partly contribute to the discrepancy between the simulated and experimental residual deflections, particularly at the closest stand-off distance of 50 mm, where the deformation, strain-rate effect, and stress state are the most severe. Future work may further incorporate multi-directional tensile and compressive tests, as well as orthotropic or anisotropic constitutive models, to quantify the influence of direction-dependent material behavior on the blast response of SLM honeycomb structures.

4.3. Filling materials

The PU filling plays an important role in the blast resistance of the HSS by providing both structural support and additional energy dissipation. Its contribution is not limited to the direct absorption of impact energy; more importantly, it interacts with the metallic honeycomb core and improves the stability of the core during progressive collapse. The enhancement effect of the PU filling can be mainly attributed to the following mechanisms:

(i) Lateral support and buckling stabilization: The PU filling occupies the honeycomb cells and provides lateral support to the thin metallic cell walls. This support restrains premature local buckling and promotes a more progressive folding deformation of the honeycomb core. As a result, the blast load can be redistributed over a larger deformation region, and the energy absorption process becomes smoother and more stable.

(ii) Viscoelastic and microcellular energy dissipation: Under high-strain-rate compression, the PU matrix exhibits pronounced viscoelastic hysteresis. Meanwhile, the compression and collapse of the internal microcells further dissipate impact energy through cell-wall bending, collapse, and gas compression. These mechanisms enable the PU filling to absorb a considerable amount of energy while maintaining partial integrity during large compressive deformation.

(iii) Metal–polymer interfacial friction: During the deformation of the HSS, relative sliding and friction occur between the metallic honeycomb walls and the PU filling. This metal–polymer interaction forms an additional damping mechanism, which helps reduce the transmitted shock intensity and mitigates the dynamic response of the back face sheet.

Therefore, the PU filling does not merely act as an additional energy-absorbing phase. By supporting the honeycomb walls, it helps stabilize the metallic core and promotes progressive folding during collapse. In turn, the confinement provided by the honeycomb cells enhances the compressive resistance of the PU filling under high-rate loading. This mutual constraint between the metallic honeycomb and the PU filling produces a synergistic energy absorption mechanism, which is essential for reducing the back-face deformation of the HSS.

The energy analysis further supports this mechanism. Although the PU filling accounts for only 12.3% of the total mass of the HSS, it contributes 22.7–25.5% of the total absorbed energy. When normalized by mass fraction, namely by comparing the energy fraction-to-mass fraction ratios, the PU filling exhibits a specific energy absorption contribution more than 1.7 times that of the metallic honeycomb core. This indicates that the PU filling substantially improves the mass-specific energy absorption efficiency of the sandwich structure, which is beneficial for lightweight blast-resistant design.

5. Conclusion

This study combined near-field blast experiments with validated S-ALE numerical simulations to evaluate the dynamic response and energy absorption mechanisms of PU-filled SLM 316L HSS. The main conclusions are summarized as follows:

(i) PU-filled 316L stainless steel HSS specimens were successfully fabricated using SLM, achieving an integrated connection between the face sheets and the honeycomb core. Basic mechanical tests were conducted on SLM-fabricated 316L stainless steel, and the Johnson–Cook constitutive parameters were calibrated from the measured quasi-static, high-strain-rate, and elevated-temperature mechanical responses. A numerical model based on the S-ALE algorithm was then established to simulate the entire "initiation–response–energy absorption" process under near-field blast loading. The calculated residual deflections showed acceptable agreement with the experimental measurements, with relative errors within 14%, confirming that the model can reasonably capture the deformation trend of the HSS under near-field blast loading.

(ii) Both the HSS and the solid plate with equivalent areal density exhibited Mode I large plastic deformation. Compared with the solid plate, the back-face residual deflection of the PU-filled HSS was substantially reduced by 20.4%, 13.2%, and 19.3% at stand-off distances of 50 mm, 75 mm, and 100 mm, respectively, demonstrating its superior blast resistance.

(iii) The pressure analysis showed that the reflected peak pressures at scaled distances of Z = 0.1315, 0.1972, and 0.2630 $m \cdot kg^{-1/3}$ were 1757.2 MPa, 1131.9 MPa, and 762.8 MPa, respectively. Compared with the conventional spherical charge model, the cylindrical charge exhibited a significant peak amplification effect.

(iv) The energy analysis indicated that the honeycomb core and the PU filling were the primary energy-absorbing components. At a stand-off distance of 50 mm, they absorbed 45.7% and 22.7% of the total absorbed energy, respectively. Across all three stand-off distances, the honeycomb core contributed 44.6–46.3%, while the PU filling contributed 22.7–25.5%, despite its mass fraction of only 12.3%. The PU achieved high specific energy absorption through mechanisms such as micropore compression, viscoelastic hysteresis, and interfacial friction.

(v) The synergistic "plastic buckling + viscoelastic damping" effect between the metallic honeycomb and the PU filling effectively delayed local instability and enhanced the overall blast resistance and structural stability.

Acknowledgments

The authors gratefully acknowledge Prof. Mustafa Güden and Prof. Zhenan Zhao for their valuable discussions and suggestions. Special thanks are also extended to Tianjin LiM Laser Technology Co., Ltd. for their assistance in SLM fabrication.

Funding

This research was funded by the Program of National Key Laboratory of Science and Technology on Materials under Shock and Impact (No. 614902230107) and the National Natural Science Foundation of China General Project (No. 12272053).

Conflict of interest

The authors declare there are no conflicts of interest.

Author contributions

Conceptualization: Xiaoshuai Li, Chao Zhang, Jing Xie
Formal analysis: Xingran Zheng, Xiaoshuai Li
Investigation: Xingran Zheng, Jingbo Huang, Liangjun Ma
Methodology: Xingran Zheng, Jingbo Huang
Writing–original draft: Xingran Zheng
Writing–review & editing: Yangwei Wang, Pengwan Chen, Jing Xie

Ethics approval and consent to participate

Not applicable.

Consent for publication

Not applicable.

Availability of data

Datasets used and/or analyzed during the current study are available from the corresponding author upon reasonable request.

References

1. Marshall A. Sandwich construction. In: Lubin G, ed. *Handbook of Composites*. 2nd ed. New York, NY: Van Nostrand Reinhold; 1982:557-601.

   doi: 10.1007/978-1-4615-7139-1_21

2. Wadley HNG. Multifunctional periodic cellular metals. *Philos Trans R Soc A Math Phys Eng Sci.* 2006;364:31-68.

   doi: 10.1098/rsta.2005.1697

3. Yungwirth CJ, O'Connor J, Zakraysek A, Deshpande VS, Wadley HNG. Explorations of hybrid sandwich panel concepts for projectile impact mitigation. *J Am Ceram Soc.* 2011;94(suppl 1):S62-S75.

   doi: 10.1111/j.1551-2916.2011.04501.x

4. Yu B, Han B, Ni CY, Zhang QC, Chen CQ, Lu TJ. Dynamic crushing of all-metallic corrugated panels filled with closed-cell aluminum foams. *J Appl Mech.* 2015;82(1):011006.

   doi: 10.1115/1.4028995

5. Wang Y, Xu F, Gao H, Li X. Elastically isotropic truss-plate-hybrid hierarchical microlattices with enhanced modulus and strength. *Small.* 2023;19(18):e2206024.

   doi: 10.1002/smll.202206024

6. Bohara RP, Linforth S, Nguyen T, Ghazlan A, Ngo T. Anti-blast and -impact performances of auxetic structures: a review of structures, materials, methods, and fabrications. *Eng Struct.* 2023;276:115377.

   doi: 10.1016/j.engstruct.2022.115377

7. Han B, Song H, Wang Y, Zhang Q. Superior compressive behaviour of alveolar biomimetic interlaced hollow lattice metastructures. *Virtual Phys Prototyp.* 2025;20(1):e2512166.

   doi: 10.1080/17452759.2025.2512166

8. Dharmasena KP, Wadley HNG, Xue Z, Hutchinson JW. Mechanical response of metallic honeycomb sandwich panel structures to high-intensity dynamic loading. *Int J Impact Eng.* 2008;35(9):1063-1074.

   doi: 10.1016/j.ijimpeng.2007.06.008

9. Yungwirth CJ, Wadley HNG, O'Connor JH, Zakraysek AJ, Deshpande VS. Impact response of sandwich plates with a pyramidal lattice core. *Int J Impact Eng.* 2008;35(8):920-936.

   doi: 10.1016/j.ijimpeng.2007.07.001

10. Bohara RP, Linforth S, Nguyen T, Ghazlan A, Ngo T. Dual-mechanism auxetic-core protective sandwich structure under blast loading. *Compos Struct.* 2022;299:116088.

    doi: 10.1016/j.compstruct.2022.116088

11. Yazici M, Wright J, Bertin D, Shukla A. Experimental and numerical study of foam-filled corrugated core steel sandwich structures subjected to blast loading. *Compos Struct.* 2014;110:98-109.

    doi: 10.1016/j.compstruct.2013.11.016

12. Alavi Nia A, Sadeghi MZ. An experimental investigation on the effect of strain rate on the behaviour of bare and foam-filled aluminium honeycombs. *Mater Des.* 2013;52:748-756.

    doi: 10.1016/j.matdes.2013.06.006

13. Li L, Zhang F, Li J, Jia F, Han B. Computational analysis of sandwich panels with graded foam cores subjected to combined blast and fragment impact loading. *Materials (Basel).* 2023;16(12):4371.

    doi: 10.3390/ma16124371

14. Pan T, Bian XB, Yuan MZ, *et al.* Baozha chongjibo zuoyong xia ju'an zhi-banqiu jiaxin jiegou de dongtai xiangying [Dynamic response of polyurethane-hemispherical sandwich structures under blast loading]. *Acta Armamentarii.* 2023;44(12):3580-3589. [In Chinese]

doi: 10.12382/bgxb.2023.0645

15. Zhang P, Cheng YS, Liu J, *et al*. Experimental study on the dynamic response of foam-filled corrugated core sandwich panels subjected to air blast loading. *Compos Part B Eng.* 2016;105:67-81.

doi: 10.1016/j.compositesb.2016.08.038

16. Cheng YS, Liu MX, Zhang P, *et al*. The effects of foam filling on the dynamic response of metallic corrugated core sandwich panel under air blast loading: experimental investigations. *Int J Mech Sci.* 2018;145:378-388.

doi: 10.1016/j.ijmecsci.2018.07.030

17. Vaziri A, Xue Z, Hutchinson JW. Metal sandwich plates with polymer foam-filled cores. *J Mech Mater Struct.* 2006;1(1):97-127.

doi: 10.2140/jomms.2006.1.97

18. Li XS, Huang JB, Xie J, Li JF, Xu ZJ, Chen PW. Lianjie fangshi dui fengwo jiaxin jiegou kangbao xingneng de yingxiang guilü yanjiu [Influence of connection mode on blast resistance of honeycomb sandwich structures]. *Packaging Engineering.* 2024;45(19):29-40. [In Chinese]

doi: 10.19554/j.cnki.1001-3563.2024.19.002

19. Casati R, Lemke J, Vedani M. Microstructure and fracture behavior of 316L austenitic stainless steel produced by selective laser melting. *J Mater Sci Technol.* 2016;32(8):738-744.

doi: 10.1016/j.jmst.2016.06.016

20. Mertens A, Reginster S, Contrepois Q, Dormal T, Lemaire O, Lecomte-Beckers J. Microstructures and mechanical properties of stainless steel AISI 316L processed by selective laser melting. *Mater Sci Forum.* 2014;783-786:898-903.

doi: 10.4028/www.scientific.net/MSF.783-786.898

21. Leicht A, Klement U, Hryha E. Effect of build geometry on the microstructural development of 316L parts produced by additive manufacturing. *Mater Charact.* 2018;143:137-143.

doi: 10.1016/j.matchar.2018.04.040

22. Niendorf T, Leuders S, Riemer A, Richard HA, Tröster T, Schwarze D. Highly anisotropic steel processed by selective laser melting. *Metall Mater Trans B.* 2013;44(4):794-796.

doi: 10.1007/s11663-013-9875-z

23. Kurzynowski T, Gruber K, Stopyra W, Kuźnicka B, Chlebus E. Correlation between process parameters, microstructure and properties of 316L stainless steel processed by selective laser melting. *Mater Sci Eng A.* 2018;718:64-73.

doi: 10.1016/j.msea.2018.01.103

24. Güden M, Yavaş H, Tanrıkulu AA, *et al*. Orientation dependent tensile properties of a selective-laser-melted 316L stainless steel. *Mater Sci Eng A.* 2021;824:141808.

doi: 10.1016/j.msea.2021.141808

25. Suryawanshi J, Prashanth KG, Scudino S, Eckert J, Prakash O, Ramamurty U. Simultaneous enhancements of strength and toughness in an Al–12Si alloy synthesized using selective laser melting. *Acta Mater.* 2016;115:285-294.

doi: 10.1016/j.actamat.2016.06.009

26. Smith LC. *On the Dynamic Response of Additively Manufactured 316L Stainless Steel and the Development of an Orthotropic Johnson–Cook Viscoplastic Strength Model.* PhD thesis. Oxford, UK: University of Oxford; 2023.

27. Liu H, Huang RY, Jiang D, Qin J, Wen YB, Zhang YZ. Yingzhi ju'an zhi paomo suliao de yingbianlü xiaoying yanjiu [Strain rate effect of rigid polyurethane foam]. *J Mech Eng.* 2023;59(16):192-203. [In Chinese]

doi: 10.3901/JME.2023.16.192

28. Koohbor B, Kidane A, Lu WY, Sutton MA. Investigation of the dynamic stress–strain response of compressible polymeric foam using a non-parametric analysis. *Int J Impact Eng.* 2016;91:170-182.

doi: 10.1016/j.ijimpeng.2016.01.007

29. Whisler D, Kim H. Experimental and simulated high strain dynamic loading of polyurethane foam. *Polym Test.* 2015;41:219-230.

doi: 10.1016/j.polymertesting.2014.12.004

30. Li X, Roth CC, Tancogne-Dejean T, Mohr D. Rate- and temperature-dependent plasticity of additively manufactured stainless steel 316L: characterization, modeling and application to crushing of shell-lattices. *Int J Impact Eng.* 2020;145:103671.

doi: 10.1016/j.ijimpeng.2020.103671

31. Zhao ZY, Jiang H, Li XD, Zhang XD, Su X, Zou MS. Research on the dynamic compressibility of polyurethane microcellular elastomer and its application for impact resistance. *Chin J Polym Sci.* 2024;42(8):1185-1197.

doi: 10.1007/s10118-024-3134-4

32. Si D, Pan Z, Zhang H. Determination method of mesh size for numerical simulation of blast load in near-ground detonation. *Defence Technol.* 2024;38:111-125.

doi: 10.1016/j.dt.2023.08.004

33. Henrych J. *The Dynamics of Explosion and Its Use*. Amsterdam, Netherlands: Elsevier Scientific Publishing Company; 1979.

34. Brode HL. Blast wave from a spherical charge. *Phys Fluids.* 1959;2(2):217-229.

35. Gan L, Chen L, Zong ZH, Qian HM. Jin juli baozha bili baoju de jieding biaozhun ji zaihe moxing [Definition criteria and load model of scaled distance in near-field explosion]. *Explosion Shock Waves.* 2021;41(6):064902. [In Chinese]

doi: 10.11883/bzycj-2020-0194

36. Ma RL, Wang XJ, Sun ZM, You S, Huang FL. Qiu xing he zhu xing zhuangyao jinchang baozha chongjibo zaihe texing [Characteristics of blast wave loads of spherical and cylindrical charges in near-field explosions]. *Acta Armamentarii.* 2025;46(1):24-38. [In Chinese]

doi: 10.12382/bgxb.2023.1105

37. Shin J, Whittaker AS, Cormie D. Incident and normally reflected overpressure and impulse for detonations of spherical high explosives in free air. *J Struct Eng.* 2015;141(12):04015057.

doi: 10.1061/(ASCE)ST.1943-541X.0001305

38. Karlos V, Solomos G, Larcher M. *Analysis of Blast Parameters in the Near-Field for Spherical Free-Air Explosions.* Luxembourg: Publications Office of the European Union; 2016. EUR 27823 EN.

doi: 10.2788/778898

39. Xiao W, Andrae M, Gebbeken N. Effect of charge shape and initiation configuration of explosive cylinders detonating in free air on blast-resistant design. *J Struct Eng.* 2020;146(8):04020146.

doi: 10.1061/(ASCE)ST.1943-541X.0002694

40. Pan W, Xia YY, Zhang C, Fang HY, Wang FM. Xinxing ju'an zhi tanxingti zhujiang cailiao de yasuo chicun xiaoying ji yingbianlü xiaoying [Size and strain rate effects on the compression of novel polyurethane elastomer grouting materials]. *Mater Rep.* 2023;37(15):273-279. [In Chinese]

41. Qiu C, Al Kindi M, Aladawi AS, Al Hatmi I. A comprehensive study on microstructure and tensile behaviour of a selectively laser melted stainless steel. *Sci Rep.* 2018;8(1):7785.

doi: 10.1038/s41598-018-26136-7

42. Suryawanshi J, Prashanth KG, Ramamurty U. Mechanical behavior of selective laser melted 316L stainless steel. *Mater Sci Eng A.* 2017;696:113-121.

doi: 10.1016/j.msea.2017.04.058

43. Jacob N, Nurick GN, Langdon GS. The effect of stand-off distance on the failure of fully clamped circular mild steel plates subjected to blast loads. *Eng Struct.* 2007;29(10):2723-2736.

doi: 10.1016/j.engstruct.2007.01.021

44. Jiang HZ, Li ZY, Feng T, *et al.* Effect of process parameters on defects, melt pool shape, microstructure, and tensile behavior of 316L stainless steel produced by selective laser melting. *Acta Metall Sin Engl Lett.* 2021;34(4):495-510.

doi: 10.1007/s40195-020-01143-8

Appendix

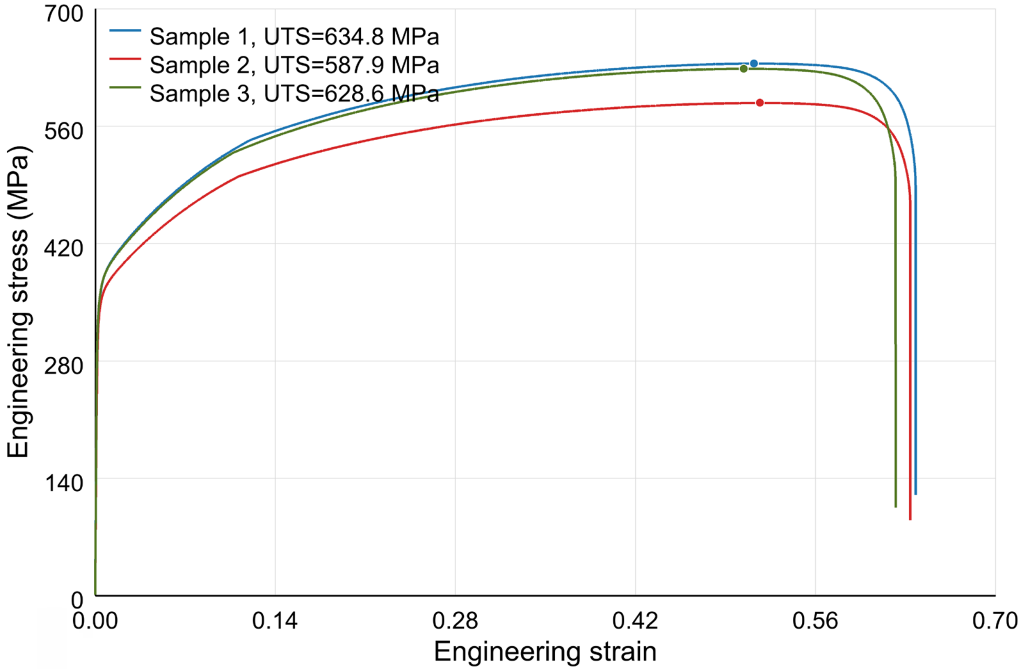

Figure A1. Engineering stress–strain curves of SLM 316L stainless steel obtained from quasi-static tensile tests
Abbreviation: UTS: Ultimate tensile strength.

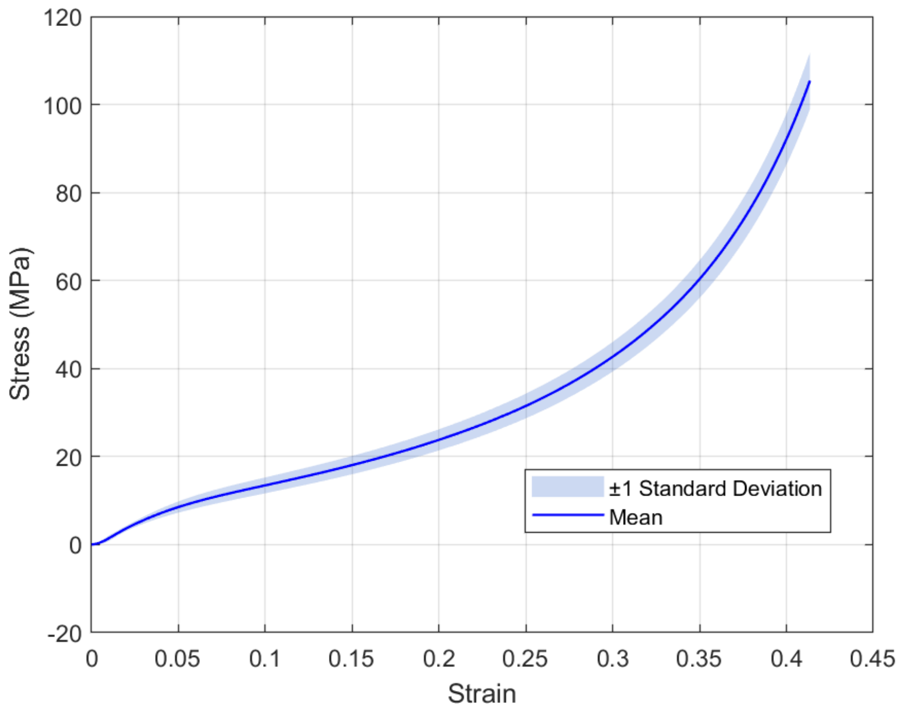

Figure A2. Quasi-static compressive stress–strain curve of polyurethane